

Limit-cycle model for internal-transport-barrier oscillations

António J. Coelho

antonio.joao.coelho@tecnico.ulisboa.pt

Instituto Superior Técnico, Lisboa, Portugal

October 2019

Abstract

A 0-D model for the time evolution of the electron temperature T and current density j is derived from the 1-D electron heat transport and current density diffusion equations. The stationary regimes of the model are analysed and it is shown that they reproduce well the cases of total diffusion (no sources), of a pure Ohmic (OH) discharge and of a constant external heating scenario. Moreover, it is seen that, as the fraction of external current applied off-axis is increased, the system moves from an OH regime into an internal transport barrier (ITB) regime, where j is reversed and the negative magnetic shear reduces the heat diffusivity, thus increasing T at the core. When the external power deposition is made proportional to both T and j , limit cycle oscillations, which resemble those of the O-regime at Tore Supra, are found. The more exact 1-D equations are then solved numerically and an oscillatory regime with features similar to the experiments is found, namely, the period of the oscillations is of the order of the resistive time scale and the decrease of the oscillations amplitude with increasing frequency is recovered.

Keywords: internal transport barriers, limit cycle oscillations, non-inductive current, advanced tokamak scenarios, negative magnetic shear

1. Introduction

The usual inductive operation of a tokamak uses a transformer to generate the toroidal current, making this mode of operation inherently pulsed and inhibiting any steady-state (SS) or long-pulsed scenarios that could deliver continuous electrical power to the grid and reduce the cost of fusion power, since the toroidal field coils no longer need to withstand the effects of cyclic fatigue [1] and hence to be replaced more frequently. Furthermore, a pulsed mode implies cyclic thermal and mechanical stresses that potentially degrade the wall materials much faster [2]. This means that an SS or a hybrid scenario, where plasma current is driven completely, or partially, by non-inductive (NI) means is one of the main goals in view of future reliable fusion reactors [1, 3]. Since, from an energetic point of view, it is economically prohibitive to rely solely on external current drive (CD) mechanisms, one must look for scenarios with a high fraction of bootstrap (BS) current [2, 3]. To achieve these scenarios, a highly tailored hollow current density profile is required, which can be created by means of some external CD applied off-axis. This will induce a reversed profile for the safety factor q , i.e., an inner zone with negative magnetic shear, or a reversed shear (RS) region, that opposes the growth of drift-wave instabilities, eventually stabilizing them. Moreover, sheared $\mathbf{E} \times \mathbf{B}$ flows can reduce the ampli-

tude of turbulent fluctuations. These two phenomena together result in a local decrease of the particle and heat turbulent diffusion coefficients, which can trigger the formation of an internal transport barrier (ITB), a region within the plasma core where the density and temperature gradients become large [1].

Whereas the radial heat and particle fluxes stay essentially the same in this region of improved confinement, the pressure in the plasma center will increase substantially, leading in this way to a higher value of the energy confinement time. This is the main reason why ITB's are a key factor in future operation of advanced tokamak (AT) scenarios. Notwithstanding this advantage, an oscillatory regime featuring long-lasting, quasi-sinusoidal electron-temperature oscillations in the core has been observed in Tore Supra (and dubbed the O-regime) [4]. These oscillations are a result of a non-linear coupling between electron temperature T and current density j and they are understood as the manifestation of an incomplete ITB transition, i.e., a regime that oscillates back and forth around a bifurcation to an enhanced core confinement state [5].

These oscillations have also appeared in fully non-inductive experiments at TCV [6] and DIII-D [7] tokamaks, although in the latter case the oscillations are more of a relaxation type rather than sinusoidal. In the Tore Supra case, the onset of the oscillations is linked

to the quasi-full lower-hybrid (LH) current drive, which introduces a strong dependence of the current diffusion on the temperature and q -profiles [8], but this coupling might also come from electron cyclotron (EC) heating and ECCD [6, 7], or even in high BS scenarios, since the BS current depends on temperature and q profiles. In all cases the oscillations have a very low frequency (1-10Hz) and are azimuthally and poloidally symmetric.

Understanding the phenomenology underlying these oscillations, as well as the equations behind it, is of great importance, since this strong coupling between current and temperature may be a common feature of SS tokamak plasmas, and so we must know how to deal with it, especially when AT scenarios are one possibility for the operation of future tokamaks. So far, these oscillations have been analysed in the framework of the TASK/TR [9], ASTRA [10], CRONOS [5, 8] and JETTO [2] transport codes, and also a link between Tore Supra's O-regime and a modified predator-prey dynamical system has been presented [5]. In this work we intend to tackle these oscillations also from a dynamical system point of view, but with a more consistent 0-D model derived from the 1-D transport equations for heat and current density. This differs from the predator-prey analysis [5] since the very simple noisy Lotka-Volterra equations used therein were introduced in an *ad-hoc* fashion and not via a more accurate reduction of the 1-D equations describing current diffusion and heat transport. Our approach is thus to look for limit-cycles (LC's), within our model, when these originate from an Andronov-Hopf bifurcation, a very common bifurcation in the study of dynamical systems, and which is the birth of a LC [11]. Subsequently, we are interested in solving the more accurate 1-D equations and compare the results with those of the 0-D model.

This paper is organised as follows. In section 2, the 0-D model is derived from the 1-D transport equations and the heat diffusivities are adapted to the model; in section 3, the 0-D model is exploited and the conditions to see ITB oscillations are given; in section 4, the 1-D model is implemented and the results are presented; finally, in section 5 we present the conclusions of this work.

2. Derivation of the 0-D model

2.1. Transport equations

The equations used in our model are the electron heat transport and the current density (or poloidal magnetic field) diffusion equations. In this work we use cylindrical geometry (valid for a tokamak with large aspect-ratio) with poloidal and axial symmetry. The equations for T and j are [5, 9]

$$\frac{3}{2}n \frac{\partial T}{\partial t} = n \frac{1}{r} \frac{\partial}{\partial r} \left(r \chi \frac{\partial T}{\partial r} \right) + S_{\Omega} + S_{\text{ext}}, \quad (1)$$

$$\mu_0 \frac{\partial j}{\partial t} = \frac{1}{r} \frac{\partial}{\partial r} \left[r \frac{\partial}{\partial r} (\eta(j - j_{\text{NI}})) \right], \quad (2)$$

where $S_{\Omega} = \eta j(j - j_{\text{NI}})$ is the OH heating, S_{ext} is the external heating, $j_{\text{NI}} = j_{\text{BS}} + j_{\text{ext}}$ is the NI current given by the sum of the BS current with the externally driven current, χ is the electron heat diffusivity and $\eta = \tilde{\eta}/T^{3/2}$ is Spitzer's resistivity with $\tilde{\eta} = 6.1 \times 10^{-8} \Omega \cdot \text{m}$ if $[T] = \text{keV}$ [12]. The electron density n is assumed to be a constant value, which is a good approximation when refueling takes place by gas puffing from the outside [12]. Finally, note that, instead of using (2), it is possible to work with the poloidal magnetic field B diffusion equation

$$\frac{\partial B}{\partial t} = \frac{\partial}{\partial r} \left[\eta \left(\frac{1}{\mu_0 r} \frac{\partial(rB)}{\partial r} - j_{\text{BS}} - j_{\text{ext}} \right) \right], \quad (3)$$

j and B being related by means of Ampère's law.

2.2. Deriving the 0-D model

The strategy is to assume quadratic profiles for $T(r)$ and $j(r)$ with the following boundary conditions (BC's): the values of T and j are fixed at the foot of the ITB, $r = r_b$, with $T(r_b, t) = T_b$ and $j(r_b, t) = j_b$. Furthermore, we require that $\partial_r T(r = 0) = \partial_r j(r = 0) = 0$. Hence, the profiles compatible with these constraints are

$$T(r, t) = T_0 - (T_0 - T_b) \left(\frac{r}{r_b} \right)^2, \quad (4)$$

$$j(r, t) = j_0 - (j_0 - j_b) \left(\frac{r}{r_b} \right)^2, \quad (5)$$

the time dependency entering via $T_0 = T_0(t)$ and $j_0 = j_0(t)$. The NI current term is treated also with a second order expansion around the ITB foot, being given by $j_{\text{NI}} = j_{\text{NI}_b} (r/r_b)^2$ with $j_{\text{NI}_b} = j_{\text{BS}_b} + j_{\text{ext}_b}$. So, after inserting these profiles in (1) and (2), and evaluating both equations at $r = 0$, the two coupled PDE's become a non-linear autonomous dynamical system, namely,

$$\begin{aligned} \frac{3}{2}n \left(\frac{\partial_t T_0}{T_b} \right) &= -\frac{4n\chi}{r_b^2} \left(\frac{T_0}{T_b} - 1 \right) + \\ &+ \frac{\eta_b j_b^2}{T_b} \left(\frac{T_b}{T_0} \right)^{3/2} \left(\frac{j_0}{j_b} \right)^2 + \frac{S_{\text{ext}}(r=0)}{T_b}, \end{aligned} \quad (6)$$

$$\begin{aligned} \mu_0 \left(\frac{\partial_t j_0}{j_b} \right) &= 2 \left\{ \frac{3\eta_b}{r_b^2} \left(\frac{T_0}{T_b} - 1 \right) \left(\frac{T_b}{T_0} \right)^{5/2} \frac{j_0}{j_b} - \right. \\ &\frac{2\eta_b}{r_b^2} \left(\frac{T_b}{T_0} \right)^{3/2} \left(\frac{j_0}{j_b} - 1 \right) \left. \right\} - \\ &- 4 \frac{\eta_b}{r_b^2} \left(\frac{T_b}{T_0} \right)^{3/2} \left\{ \frac{j_{BS_b}}{j_b} + \frac{j_{ext_b}}{j_b} \right\}. \end{aligned} \quad (7)$$

The time-varying value of the BS current at the barrier's foot j_{BS_b} is evaluated using Eq. (4.9.2) in [13] and profiles (4) and (5). After some simple algebra we get

$$j_{BS_b} [\text{A/m}^2] = 3.5 \times 10^4 \frac{n_{20}}{\mu_0 R_0^{1/2} r_b^{3/2}} \frac{T_0 - T_b}{j_0 + j_b}. \quad (8)$$

Regarding the external current, we fix $j_{ext_b}/j_b \equiv K_{NI}$ to a constant value. Finally, we define the adimensional quantities $x \equiv T_0/T_b$ and $y \equiv j_0/j_b$, which become quite useful in what follows.

2.3. Models for the heat diffusivity

The only quantity in (6) and (7) we have not yet provided is the electron heat diffusivity χ . Currently, a first-principles derived heat diffusivity taking into account the negative magnetic shear effect is still lacking. Indeed, transport simulations typically use an heuristic model that mimics the reduction of the coefficients in the presence of an RS configuration [8, 14]. In the present work we will use two different forms for the diffusivity. The first one is a phenomenological model that captures the essence of the influence the shear s has in reducing χ : for $s < 0$, the heat diffusivity tends to a lower value (χ_H , high confinement mode), and for $s > 0$ to a higher value (χ_L , low confinement mode). By casting this behaviour in a logistic function, the henceforth mentioned ‘‘shear diffusivity’’ is given by

$$\chi_{sh} = \chi_H + \frac{\chi_L - \chi_H}{1 + e^{-\alpha s}} \quad (9)$$

with α a shear control parameter. Because the shear is a complicated function of j , it is important to realize that, within our model, $y > 1$ corresponds to a typical OH non-reversed discharge, whereas $y < 1$ corresponds to a reversed shear configuration. Thus, we would have the correspondence: as $y \rightarrow 0$, $\chi \rightarrow \chi_H$ and as $y \rightarrow +\infty$, $\chi \rightarrow \chi_L$:

$$\chi_{sh} = -2 \frac{\chi_H - \chi_L}{1 + e^{-\alpha y}} + 2\chi_H - \chi_L. \quad (10)$$

Note that this expression is only valid for $y \geq 0$, since for $y < 0$ the expression may become negative. We will now fix $\chi_H = 0.1 \text{ m}^2/\text{s}$ and $\chi_L = 1.0 \text{ m}^2/\text{s}$ since typically the turbulent diffusion coefficients are of order

$1.0 \text{ m}^2/\text{s}$ [12] and we assume that negative magnetic shear can potentially reduce them up to one order of magnitude [5].

The second form for the diffusivity used in this work is a more sophisticated model that also takes into account temperature, as it is usual for a fusion diffusion coefficient. Without an RS configuration, turbulent diffusion coefficients usually follow the Bohm (χ_B) and gyro-Bohm (χ_{gB}) form given by

$$\chi_B = C_1 \frac{a}{B_0} q^2 \left| \frac{dT}{dr} \right|, \quad (11)$$

$$\chi_{gB} = C_2 \frac{\sqrt{T}}{B_0^2} \left| \frac{dT}{dr} \right|, \quad (12)$$

where $C_{1,2}$ are numerical coefficients usually adjusted by benchmarking a broad range of discharges, and the total diffusion coefficient is given by $\chi = \chi_B + \chi_{gB}$ [15]. Whenever the shear effect is to be taken into account, a shear function $F(s)$ multiplies the Bohm term, $\chi = \chi_{gB} + \chi_B F(s)$, so that its value is reduced in an RS configuration [8, 14]. The Bohm term is related with the long-wavelength turbulence transport and it is this one that is reduced by low-positive or negative magnetic shear; short wavelength turbulence, which produces gyro-Bohm transport, is not modified in such a region. Using profiles (4) and (5), and evaluating the diffusivity inside the barrier at $r = r_b$,¹ we get

$$\chi_B = C_1 \underbrace{\frac{2aB_0}{r_b} \left(\frac{4}{R_0 \mu_0 j_b} \right)^2}_{C'_1} T_b \frac{|x-1|}{(y+1)^2}, \quad (13)$$

$$\chi_{gB} = C_2 \underbrace{\frac{2\sqrt{T_b}}{B_0^2 r_b}}_{C'_2} T_b |x-1|. \quad (14)$$

For Tore Supra values, $R_0=2.4 \text{ m}$, $a=0.7 \text{ m}$, $r_b=0.2a$, $B_0=3.8 \text{ T}$, $n_{20} = 0.5 \text{ m}^{-3}$, $T_b=4 \text{ keV}$, $\eta_b=8 \times 10^{-9} \Omega \cdot \text{m}$, $j_b=1.5 \text{ MA/m}^2$ [5], and thus $C'_1 = 119$ and $C'_2 = 7.91$. When all constants are given in SI, except for T_b , which is given in keV, $C_1 = 0.200$ and $C_2 = 0.158$ for electrons [15]. This means that $C_1 C'_1 = 23.8 \text{ m}^2/\text{s}$, $C_2 C'_2 = 1.26 \text{ m}^2/\text{s}$. Introducing now a shear function that multiplies both Bohm and gyro-Bohm terms in order to amplify its effect, as is done in [8], we write

$$\chi_{BgB} = (\chi_{gB} + \chi_B) [1 - (1 - \gamma)e^{-\alpha y}], \quad (15)$$

with the γ -factor preventing $\chi_{BgB} \rightarrow 0$ when $y \rightarrow 0$. Thus, if for instance $\gamma = 0.01$, the total diffusivity is reduced by two orders of magnitude as $y \rightarrow 0$.

¹The reason why we do not evaluate it at the core, $r = 0$, is because (11) and (12) are zero at this position, meaning that we would lost the heat diffusion term in our model.

2.4. Nondimensionalization of the 0-D model

By defining $\tau_x = r_b^2/\chi_0$, $\tau_y = \mu_0 r_b^2/\eta_b$, $C_\Omega = 4.20 \times 10^{-5} r_b^2 \eta_b j_b^2/n_{20} T_b \chi_0$, $C_{BS} = 3.5 \times 10^4 n_{20} T_b/\mu_0 R_0^{1/2} r_b^{3/2} j_b^2$ and $(2r_b^2/3nT_b\chi_0) S_{\text{ext}}(r=0) = K_{\text{ext}} h(x, y)$, Eqs. (6) and (7) can be written in adimensional form as

$$\tau_x \dot{x} = -\frac{8}{3} \tilde{\chi}(x, y)(x-1) + C_\Omega \frac{y^2}{x^{3/2}} + K_{\text{ext}} h(x, y), \quad (16)$$

$$\tau_y \dot{y} = \frac{4}{x^{3/2}} \left[\frac{3}{2} \frac{y}{x} (x-1) - (y-1) - C_{BS} \frac{x-1}{y+1} - K_{\text{NI}} \right], \quad (17)$$

with $\tilde{\chi} \equiv \chi/\chi_0$, χ given by (10) or (15) and χ_0 a normalization constant equal to χ_L or $C_1 C_1'$, respectively. Using Tore Supra values, we have that $C_{BS} = 0.305$, $\tau_y = 3.08$ s, $\tau_x = 1.96 \times 10^{-2}$ or 8.24×10^{-4} s and $C_\Omega = 7.41 \times 10^{-3}$ or 3.11×10^{-4} , depending on the chosen χ .

It is tempting to regard τ_x and τ_y as the heat transport and current diffusion time scales, respectively. If this poses no problem with the latter, regarding the former there is a very strong dependency on the model chosen for χ , which may lead to very disparate figures for τ_x , as we have just seen. As such, we will no longer look at τ_x as being fixed by the χ model, but we will consider it an independent parameter instead, to be gauged against τ_y through the ratio $\mu \equiv \tau_x/\tau_y$. Finally, note that α , K_{NI} and K_{ext} are free parameters of the model and $h(x, y)$ is a function that may, or may not, depend on x and y , providing which external heating scheme is under consideration.

3. Results of the 0-D model

3.1. Analysis of the simplest cases

The best way to test our model is to make sure that the outcome is correct when looking at familiar situations. We thus start by studying the dynamical system in its simplest form (no sources) and then by successively adding more terms.

a) No sources

Let us thus start to set all heating and current sources to zero in (16) and (17), i.e., $C_\Omega = K_{\text{ext}} = C_{BS} = K_{\text{NI}} = 0$. In this case, the system has the fixed point $\{x_{\text{SS}} = 1, y_{\text{SS}} = 1\}$, which is a stable node regardless of the form of the diffusivity used. This result is consistent with our knowledge of transport equations: with no sources, the temperature and the current simply diffuse away, achieving a SS where T and j are equal to the boundary value everywhere - note that because T and j are normalized to the boundary values ($x = T_0/T_b$ and $y = j_0/j_b$), this SS corresponds to $x = 1$ and $y = 1$, as can be seen in Fig. 1(a). Note that the trajectory is rapidly attracted to the x-

nullecline² and then slowly approaches the stable equilibrium; this is due to the distinct time scales we have set for this simulation. In addition, keep in mind that any SS equilibrium, $\{x_{\text{SS}}, y_{\text{SS}}\}$, is independent of the time scales.

b) Effect of OH heating

If $C_\Omega \neq 0$, the stable node is $\{x_{\text{SS}} > 1, y_{\text{SS}} > 1\}$ as can be seen in Fig. 1(b), which is also consistent because, whenever there is a source term balancing the losses by diffusion, in principle it is possible to sustain non-constant temperature and current profiles. However, if the initial y , $y(0)$, is too large, the system diverges ($x \rightarrow \infty, y \rightarrow \infty$). This is simply due to the fact that OH heating scales with y^2 ; thus, if the initial y is too large, the heating will quickly overcome the diffusion losses (in the case that $\dot{x}(0) < 0$, otherwise the losses are initially already overcome), driving the system to higher and higher temperatures. On the other hand, the reason for y not stabilizing can be explained by re-writing (17) in the no-source case as

$$\dot{y} = \frac{4}{x^{3/2}} \left[\frac{y}{2} \left(1 - \frac{3}{x} \right) + 1 \right], \quad (18)$$

which shows that y will not stabilize if $x > 3$.

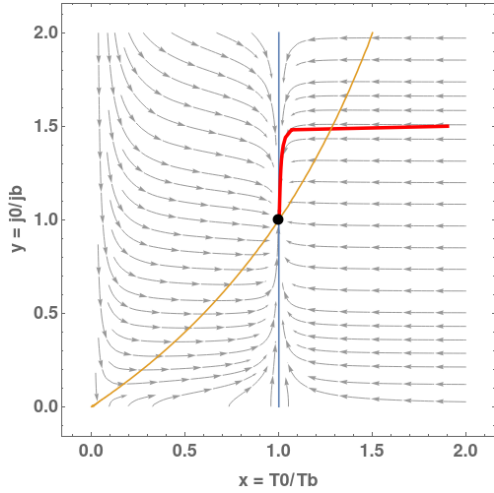
c) Effect of the NI current source terms

Let us now release the constraint $C_{BS} = 0$ and recall that in highly bootstrapped tokamak plasmas, when the BS current gets peaked off-axis, the total current density will follow it and, eventually, will also get peaked at the same position. In our 0-D model that would mean that, if we have an initial situation with $y > 1$ and at some point j_{BS} starts to increase, the total current density would start changing to a more RS profile, i.e., y would start decreasing, eventually reaching $y < 1$ if the BS term at the barrier is further increased. With this in view, observe that, from (17), an increase in the BS term will always contribute to reduce $\dot{y}(t)$; moreover, we have found that the SS y -value decreases with increasing C_{BS} . These two features of our model are thus in good agreement with what we just saw that usually happens in tokamak plasmas. Finally, note that when we allow $K_{\text{NI}} \neq 0$, we have the same effect as allowing $C_{BS} \neq 0$. Thus, if both C_{BS} and K_{NI} do not vanish, more easily y_{SS} reaches a lower value.

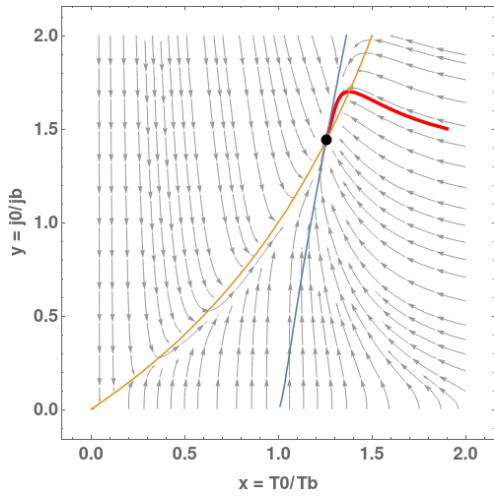
d) Effect of the external heating term

If we now set $h(x, y) = 1$ and K_{ext} a positive constant, we can find the behaviour of the system when it is externally heated at the core. It was found that there is a stable node for $0 < K_{\text{ext}} < K_{\text{ext}}^{\text{MAX}}$, and beyond $K_{\text{ext}}^{\text{MAX}}$ the nullclines no longer cross and the system diverges independently of the initial condition.

²The x- and y-nullclines are the set of points where \dot{x} and \dot{y} are zero, respectively.



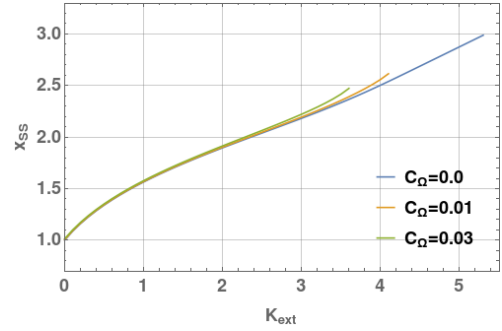
(a) $C_\Omega = 0$ and $\mu = 0.001$.



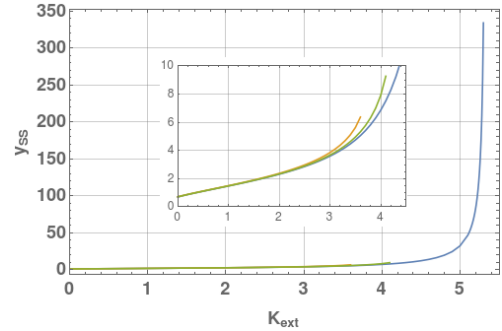
(b) $C_\Omega = 0.02$ and $\mu = 0.1$.

Figure 1: Phase space and vector field of (16) and (17) with $\chi = \chi_{\text{BgB}}$, $\alpha = 1.0$ and $K_{\text{ext}} = K_{\text{NI}} = 0$. Blue and orange lines are the x- and y-nullclines, respectively. Red curve is some trajectory in the phase space and the black dot indicates the stable fixed point $\{x_{\text{SS}}, y_{\text{SS}}\}$. Note that, whatever the initial conditions are, the system evolves always towards its stable node.

In the *convergence region*, the value of x_{SS} increases with K_{ext} , which means that more external heating leads to a higher core SS temperature. The value of y_{SS} will also increase with K_{ext} . In fact, y_{SS} increases much faster than x_{SS} with K_{ext} as can be seen in Fig. 2, where it is depicted the evolution of x_{SS} and y_{SS} with K_{ext} for three different values of C_Ω . It is possible to see that with increasing C_Ω , $K_{\text{ext}}^{\text{MAX}}$ decreases; in other words, if the OH heating increases, there is “less space” for the system to be externally heated without diverging. Moreover, the highest x_{SS} value increases with decreasing C_Ω ; in the limit $C_\Omega \rightarrow 0$, the highest



(a)



(b)

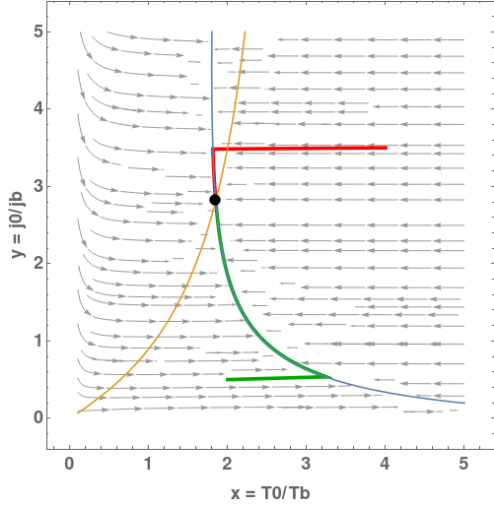
Figure 2: Stable fixed points x_{SS} and y_{SS} , (a) and (b) respectively, as functions of K_{ext} for different C_Ω and with $\chi = \chi_{\text{sh}}$, $\alpha = 1.0$, $C_{\text{BS}} = 0.1$ and $K_{\text{NI}} = 0.3$.

value of $x_{\text{SS}} \rightarrow 3$ and $y_{\text{SS}} \rightarrow \infty$, which is consistent with what we have seen in b).

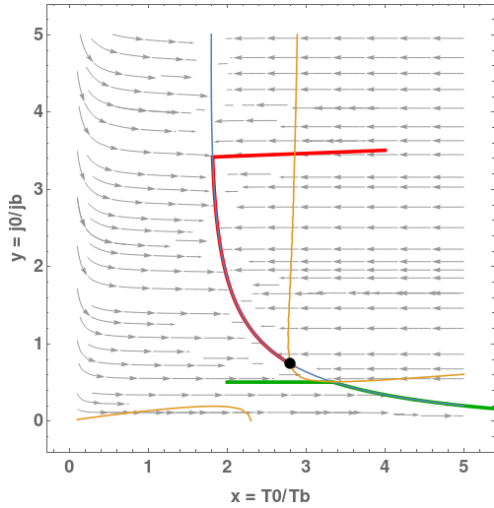
3.2. Analysis of ITB regimes

In the $h(x, y) = 1$, $K_{\text{ext}} > 0$ and $K_{\text{NI}} > 0$ case, it should be possible to observe two different SS regimes: an OH and an ITB, depending on the external parameters K_{ext} and K_{NI} , and independently of the diffusivity used, χ_{sh} or χ_{BgB} . Whereas in an OH situation we expect $x_{\text{SS}} \gtrsim 1$ and $y_{\text{SS}} \gtrsim 1$, in the case of an ITB with RS we should find $x_{\text{SS}} \gg 1$ and $y_{\text{SS}} \lesssim 1$.

The phase space corresponding to an OH and an ITB SS regime is shown in Figs. 3(a) and Fig. 3(b), respectively, where K_{ext} is fixed, but the fraction of externally applied current at the foot of the barrier, K_{NI} , is different. Then, in Fig. 4, we plot x_{SS} and y_{SS} as a function of K_{NI} and for different K_{ext} . The first thing to notice is that, in general, x_{SS} increases with K_{NI} , which means that, as the fraction of external current applied at the foot of the barrier increases, so does the temperature; this is just a consequence of y_{SS} being decreasing, reducing this way the diffusivity. Thus, we can conclude that, as K_{NI} is increased, the system moves from an SS OH regime into an SS ITB regime, i.e., a regime where the externally applied current changes the current density into a reversed profile, reducing the turbulent transport and thus allowing for



(a) SS OH regime with $K_{NI} = 0.10$.



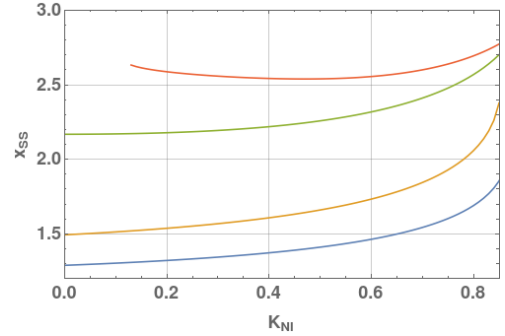
(b) SS ITB regime with $K_{NI} = 0.87$.

Figure 3: Phase space and vector field of (16) and (17) with $C_{\Omega} = 0.01$, $\mu = 0.01$, $C_{BS} = 0.1$, $\chi = \chi_{sh}$, $\alpha = 1.0$, $h(x, y) = 1$ and $K_{ext} = 2.9$. Blue and orange lines are the x- and y-nullclines, respectively. Red and green curves correspond to trajectories with different initial conditions and the black dot indicates the stable fixed point $\{x_{SS}, y_{SS}\}$.

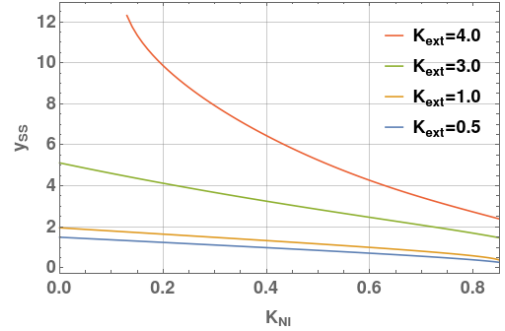
steeper temperature gradients at the core.

3.3. ITB oscillations

Regarding current and temperature oscillations, as already mentioned, these are due to the non-linear coupling between the equations that model their evolution. This coupling comes about via Spitzer's resistivity, heat diffusivity, bootstrap current and external current (and respective power deposition). The first two coupling sources (resistivity and diffusivity) are not sufficient, at least within our model, to trigger os-



(a)



(b)

Figure 4: Stable fixed points x_{SS} and y_{SS} , (a) and (b) respectively, as a function of K_{NI} for different K_{ext} and with $h(x, y) = 1$, $\chi = \chi_{sh}$, $\alpha = 1.0$, $C_{BS} = 0.1$ and $C_{\Omega} = 0.01$.

cillations. A scan in K_{ext} , K_{NI} and α (and also in μ for reasons that will become clearer in a moment) was made to look for LC's, and the result was null for both diffusivities being considered so far. This indicates that the external current density and/or its power deposition should be x and y dependent, in order to introduce a new form of coupling. In the LH case, wave propagation and absorption are usually well described by ray-tracing or full-wave codes. Obviously we are not interested in that type of approach, so we must stick to the simple scalings. Since it has been reported that the local LH absorption increases with electron temperature, whereas the global LH efficiency increases with plasma current [8], it is reasonable to assume $S_{ext} \propto jT$. This cross term between T and j is not new since it has already been used in the context of the CRONOS transport code [4, 8]. However, it had been used to model j_{LH} inside the barrier, and not the external heating profile, but since the latter typically follows the former, it is a good approximation to make the opposite way around. Thus, we will keep the fraction of externally applied current at the foot of the barrier, K_{NI} , as a constant, and write the external heating term due to LH-waves as $h(x, y) = xy$.

a) LC oscillations when $\chi = \chi_{sh}$

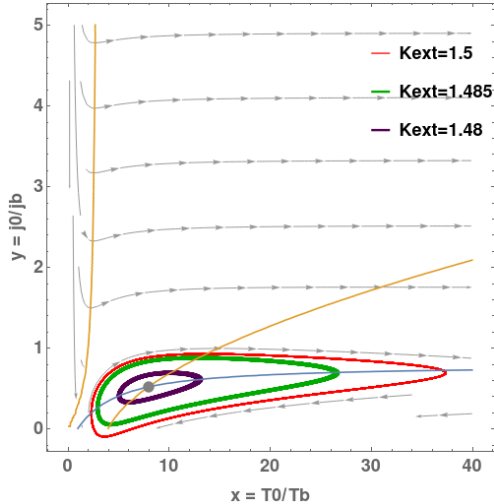


Figure 5: Phase space and vector field of (16) and (17) with $C_\Omega = 0.01$, $\mu = 1.0$, $\chi = \chi_{sh}$, $\alpha = 1.0$, $K_{NI} = 0.7$ and $h(x, y) = xy$. In this plot, we ignore the initial instants where the trajectories, coming from different initial conditions, approach the respective LC's. Blue and orange lines are the x- and y-nullclines, respectively, and the grey dot corresponds to the unstable fixed point in the $K_{ext} = 1.48$ case.

When the shear diffusivity (10) is used and α is set to 1.0, supercritical Andronov-Hopf bifurcations (stable LC's) are found for $0 < K_{NI} < 1.0$ and, for each value of K_{NI} , K_{ext} above K_{ext}^* , which is the value of K_{ext} at the bifurcation point. Furthermore, these oscillations only appear if the time-scale ratio verifies $\mu \approx 1$. In Fig. 5 we show the phase space of some of these LC's for different values of K_{ext} and $K_{NI} = 0.7$. Note that, as K_{ext} increases, so does the size of the limit cycle, as predicted for Andronov-Hopf bifurcations [11]. Note that, as K_{ext} increases, $y(0)$ and $x(0)$ cannot be too large otherwise the system is not attracted to the LC, but rather diverges away. This is simply due to the external heating being proportional to xy .

b) LC oscillations when $\chi = \chi_{BgB}$

When the BgB heat diffusivity (15) is used, supercritical Andronov-Hopf bifurcations are found when $K_{NI} > 0.5$ and, for each value of K_{NI} , K_{ext} above the bifurcation point. However, for this to occur, α must lie between roughly 0.1 and 0.01, otherwise no stable/physical LC's are found. When the values of K_{ext} and K_{NI} are not in the LC range, SS ITB regimes are encountered, which are much more pronounced than those of the constant external heating case, in the sense that $x_{SS} \gg 1$ and $y_{SS} \ll 1$. Besides, no LC's are found when the BgB heat diffusivity is used without the shear correction, nor when the BS term is disregarded, and, once more, the oscillations only appear when we set

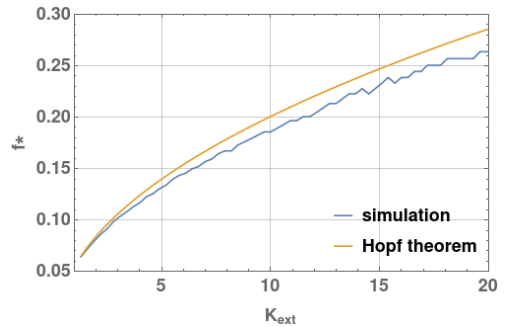


Figure 6: Normalized frequency ($f^* = f/\tau_y^{-1}$) of the LC as a function of K_{ext} for $C_\Omega = 0.001$, $C_{BS} = 0.1$, $\mu = 1.0$, $\chi = \chi_{BgB}$, $\alpha = 0.01$, $K_{NI} = 0.6$ and $h(x, y) = xy$. Simulation frequency is compared with the one given by Hopf theorem which is only exact near $K_{ext} = 1.30$ in this case.

$\mu \approx 1$. From a dynamical system point of view this is understandable: in order to have an oscillatory regime, one needs the two quantities competing with each other (just like in a predator-prey system) and this is only possible if both evolve in the same time scale. From a plasma point of view, this means one of three things: the heat transport time τ_x increases to the order of the current diffusion time τ_y , the latter decreases to the order of the former, or a mixing between these two. This last option seems very plausible because, locally close to the ITB, we expect the confinement time to substantially increase and the current diffusion time to be low (due to the small ITB radius), and thus these two times approach each other.

The oscillation frequency in our model is of the order $0.1/\tau_y$ [Hz] as can be seen in Fig. 6 where we plot the frequency normalized to τ_y^{-1} , f^* , as a function of K_{ext} . We also show the *theoretical* frequency given by the Hopf theorem, which is exact at the bifurcation point and correct within $\mathcal{O}(K_{ext} - K_{ext}^*)$ for K_{ext} close to K_{ext}^* [11]; this is the reason why this *theoretical* value is only in very good agreement with the frequency obtained with the simulation in the beginning, close to K_{ext}^* (which in the case of $K_{NI} = 0.6$ as in the figure is $K_{ext}^* = 1.30$). This order of magnitude obtained for f^* means that the the period of oscillation is of order $10\tau_y$, which is roughly one order of magnitude above what is seen in the various experiments, i.e., typically the oscillation goes with the resistive time scale [4, 5, 6, 8].

4. Implementation and results of the 1-D model

Although the 0-D model has given us a great insight into the transport equations, providing us with a very simple tool to look at stationary and oscillatory ITB regimes, we consider that three central questions should still be addressed in the more complete 1-D model, namely, the question on the time scales of

the two equations, on the oscillation frequency and on how the amplitude depends on it. For that reason, it is our purpose now to solve the 1-D equations with the same type of assumptions made within the 0-D: second-order profile for the external current density between the core and the foot of the barrier, fixed values of temperature and current density at the foot of the barrier and a phenomenological model for the heat diffusivity that takes into account its reduction in RS scenarios.

4.1. Numerical implementation

The 1-D equations to be numerically solved are (1) and (3). The reason why we now prefer to use (3) instead of (2) is that, when using model (9) for the diffusivity, we will need to have access to $s = 1 - r\partial_r B_\theta(r)/B_\theta(r)$, which is directly given by differentiation of B_θ , while if we use j we would have to perform an integration, which is not so straightforward nor intuitive when working with finite differences as we do.

The spatial derivatives of the equations are discretized using second-order finite differences, and the system is evolved in time according to a semi-implicit numerical scheme [16], which is marginally stable, and will allow to see the oscillatory regime when we make $S_{\text{ext}} \propto jT$. Would we use the typical schemes used to solve diffusion-like PDE's, such as the Crank-Nicolson scheme, the time evolution would become unstable in such scenario.

4.2. OH and ITB SS regimes

Let us analyse the SS regimes of the 1-D equations when $\chi = \chi_{\text{sh}}$, as given by the phenomenological model in (9), $S_{\text{ext}} \propto K_{\text{ext}}$ is constant and $j_{\text{ext}}(r) = K_{\text{NI}}j_b r^2$. In Fig. 7 we show an SS regime, i.e., we have given some initial profile to the numerical scheme and then evolved in time until the profile was no longer changing, with $K_{\text{NI}} = 0.8$ and $K_{\text{ext}} = 0.4$. Moreover, with two different $\{K_{\text{ext}}, K_{\text{NI}}\}$ sets, and by picking up the values of temperature and current density at $r = 0$ at each instant of time until the SS is achieved, we show the phase space in Fig. 8. Note that the cases displayed therein start at the same initial position in the phase space, but in the case where K_{NI} is much larger, the SS value of y decreases to a much lower value as expected.

We now evaluate SS profiles for different K_{ext} and with K_{NI} in the range $[0.0, 0.95]$. After doing so, we can construct the plots in Fig. 9, where x_{SS} and y_{SS} correspond to the central SS values of T and j normalized to the fixed values at the boundary, just like in the 0-D model. As expected, we see that larger heating leads to higher core temperatures, and, as the fraction of NI current applied at the foot of the barrier is increased, so does the temperature. At the same time, we see that the current density changes from an OH profile to a more reversed profile as K_{NI} increases, and that the central current density increases with K_{ext} . All this

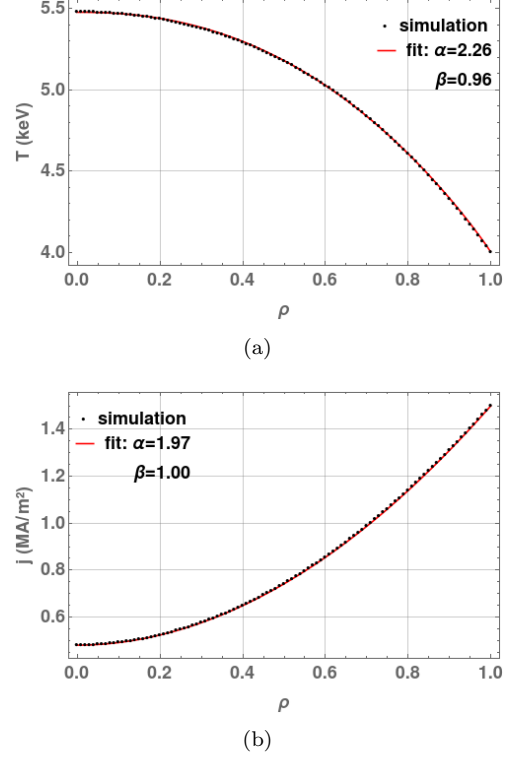


Figure 7: SS profiles of temperature (a), current density (b), poloidal magnetic field (c) and heat diffusivity (d) when $\chi = \chi_{\text{sh}}$, $\alpha = 1.0$, $K_{\text{ext}} = 0.4$ and $K_{\text{NI}} = 0.8$. A fit is made to T and j of the type $T_{\text{fit}} = T_0 + (T_0 - T_b)(1 - \rho^\alpha)^\beta$.

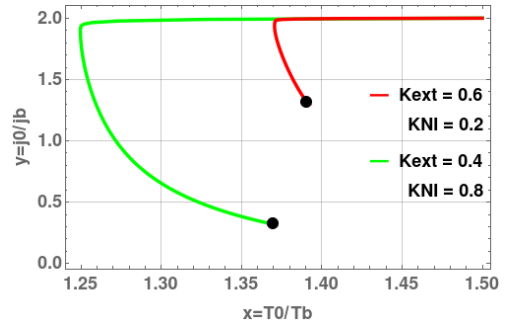


Figure 8: Phase space of $x = T_0/T_b$ and $y = j_0/j_b$ for two different $K_{\text{ext}}, K_{\text{NI}}$ conditions, but with same initial profiles. $\chi = \chi_{\text{sh}}$ and $\alpha = 1.0$. The black dots indicate the SS.

is in accordance with the results of the 0-D model - recall Fig. 4. Please note that this behaviour of changing from an OH regime into an ITB regime is induced by the type of heat diffusivity used. If χ would not have a shear dependency (for example, if it would only depend on T), the temperature equation would be decoupled from the magnetic field equation (aside from the OH heating term, which has little influence since

$K_{\text{ext}} \gg C_\Omega$), and thus x_{SS} would not be sensitive to K_{NI} .

4.3. Oscillatory regimes

When we make $S_{\text{ext}} \propto K_{\text{ext}} jT$, we do not obtain oscillatory solutions but rather stationary regimes. This suggests that we need to decouple the left-hand side of the temperature equation from the right-hand side, just like we have done in the 0-D model. That is, we need to take τ_x as an independent variable such that it approaches τ_y , since these two differ by three orders of magnitude, $\tau_x/\tau_y = 0.003$. Thus, as in section 2.4, let $\tau_x = \mu\tau_y$. In the 0-D model we have seen that oscillations only appear when $\mu \approx 1$. However, within the 1-D equations, we have also found oscillatory regimes in the $\mu \sim 0.1$ and 0.01 cases. Furthermore, contrary to the 0-D model, all the oscillatory regimes within the 1-D equations were obtained without the BS term, thus making jT the main term inducing a non-linear coupling between T and B that ultimately leads to oscillations.

The appearance of oscillations is very similar to the

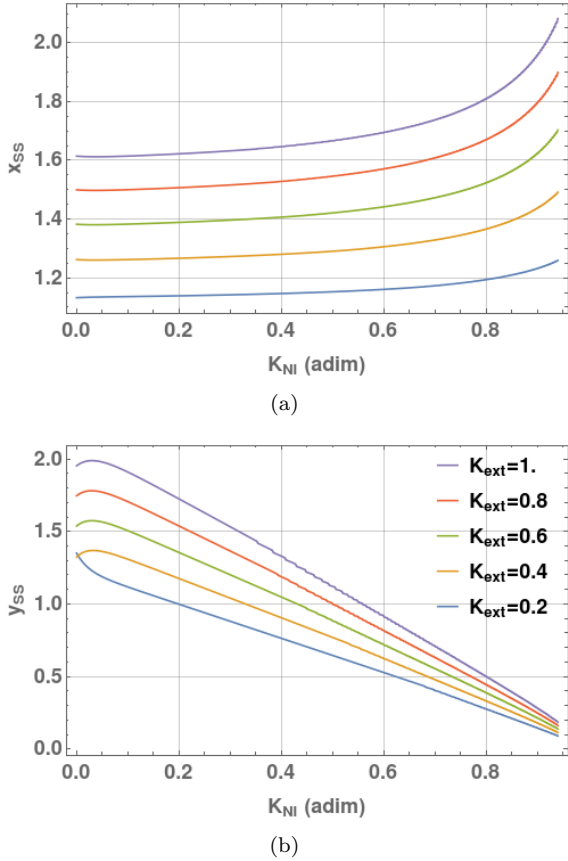


Figure 9: $x_{\text{SS}} = T_0/T_b$ and $y_{\text{SS}} = j_0/j_b$ as a function of K_{NI} for different K_{ext} and with $\chi = \chi_{\text{sh}}$ and $\alpha = 1.0$. Note that, as K_{NI} increases, the system changes from an OH regime into an ITB regime. A comparison with the 0-D model can be made through Fig. 4.

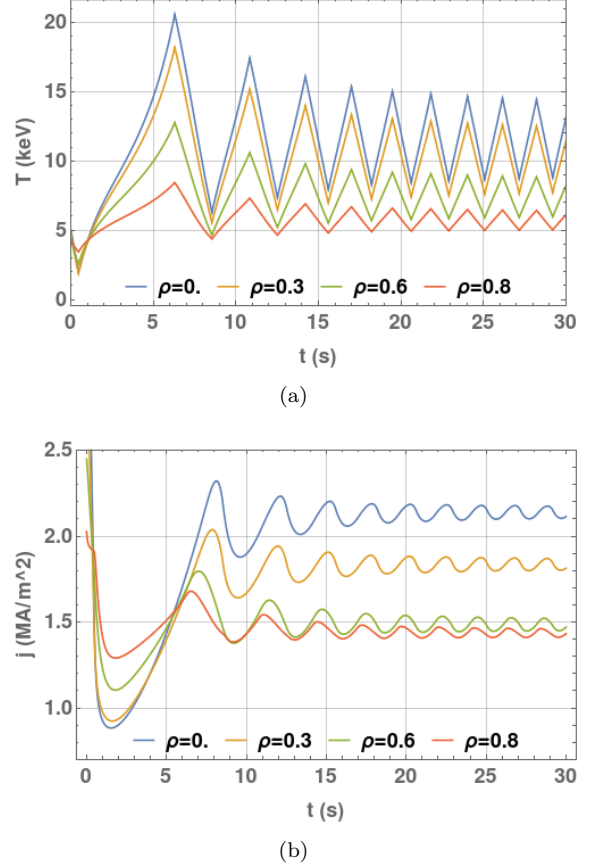


Figure 10: Temperature (a) and current density (b) oscillations at different $\rho = r/r_b$ positions when $\chi = \chi_{\text{sh}}$, $\alpha = 1.0$, $K_{\text{ext}} = 7.5$, $K_{\text{NI}} = 0.7$ and $\mu = 0.3$.

bifurcation-like behaviour we have seen in the dynamical system model: for a fixed value of K_{NI} , an oscillatory regime appears after a certain K_{ext}^* threshold. In Fig. 10 it is depicted an example of the oscillations at different $\rho = r/r_b$ positions. Note that the oscillations in j look more sinusoidal than those in T . Nevertheless, the latter resembles the O-regime in Tore Supra [4].

The oscillation's frequency was also studied in the context of the 1-D model. In Fig. 11 we show the normalized frequency $f^* = f/\tau_y^{-1}$ as function of K_{ext} and for $K_{\text{NI}} = 0.7$. It should be noted that the frequency increases with K_{ext} just like in the 0-D model, where the Hopf theorem predicts such increasing. The main difference with the 0-D model is in the frequency itself, since now we have a frequency of the order of τ_y^{-1} , or, in other words, an oscillation period of the order of τ_y , and not of $10\tau_y$ as in 0-D. The 1-D results thus agree more correctly with the experiments, since in the O-regime it was seen that the oscillation goes with the resistive time scale [4, 8]. In the same plot of Fig. 11 we depict the temperature oscillation's amplitude also as a function of K_{ext} , where it is possible to see it decreases with increasing K_{ext} . This highly contrasts with what

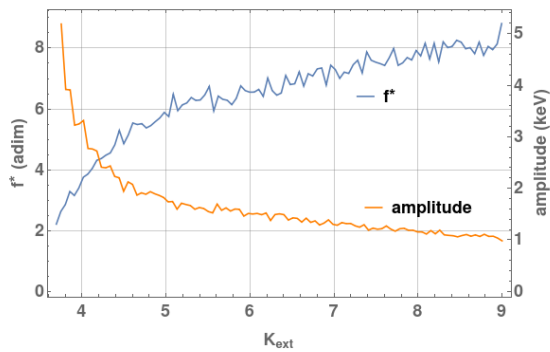


Figure 11: Normalized frequency ($f^* = f/\tau_y^{-1}$) of the LC and amplitude of the temperature oscillations as function of K_{ext} for $\chi = \chi_{\text{sh}}$, $\alpha = 1.0$, $K_{\text{NI}} = 0.7$ and $\mu = 0.3$.

was seen in the 0-D model, where an increasing was found. Nevertheless, this is exactly what happens in the O-regime at Tore Supra: decreasing of the oscillation's amplitude with increasing frequency [4].

5. Conclusions

We developed a 0-D model starting from the 1-D equations for heat transport and for the current-density diffusion. By assuming certain spatial profiles for T and j , we derived a two-dimensional dynamical system able to reproduce stationary OH and ITB regimes, the transition between these two being accomplished by increasing the fraction of external current deposited at the foot of the barrier, K_{NI} . When the external heating term of the system was further made proportional to the current density and temperature, i.e, $S_{\text{ext}} \propto jT$, in order to mimic the power deposition of an LH system, we were able to find stable LC's if the time scales that govern both equations were of the same order. There were, however, two features of the found oscillations that did not match the experimental results, namely, the oscillation's period, which was one order of magnitude above the experiment, and the LC amplitude, which increased with increasing frequency, while in the O-regime the inverse was reported. For that reason, the more exact 1-D equations were solved numerically, and by doing so we were able to conclude that: first, when the external heating is constant, $S_{\text{ext}} \propto K_{\text{ext}}$, the SS profiles are close to second-order polynomials, as assumed in the 0-D model, and the values at the core follow a similar trend with K_{ext} and K_{NI} as found in 0-D: temperature at the core increases with K_{ext} and with K_{NI} , while the value of the current density at the core decreases with K_{NI} , but increases with K_{ext} . Second, the 1-D system contains oscillatory solutions in the $S_{\text{ext}} \propto jT$ case, not only when the time scales of the two equations are of the same order, but also

when these differ by up to two orders of magnitude. This reveals that the 1-D equations are not so restrictive on the time scales as the 0-D model. Third, the oscillation's frequency scales as $(1 - 10)/\tau_y$, which is consistent with the experiments in the O-regime, where it has been reported an oscillation that goes with the resistive time scale. And finally, the oscillations' amplitude decreases with increasing frequency, which is exactly what was seen on Tore Supra [4].

Future extensions of this work, both on the 0-D and 1-D models, include introducing a non-constant density, by assuming a space-dependent profile, or by including a time-dependent equation for the density. Besides, we could also introduce an equation for the ion temperature, coupling it with the electron temperature equation via the equipartition term.

References

- [1] J. W. Connor et al., *Nucl. Fusion*, 44(4):R1, 2004.
- [2] J. P. S. Bizarro, X. Litaudon and T. J. J. Tala, *Nucl. Fusion*, 47(11):4145, 2007.
- [3] E. Joffrin, *Plasma Phys. Control. Fusion*, 49(12B):B629, 2007.
- [4] G. Giruzzi et al., *Phys. Rev. Lett.*, 91(13):14, 2003.
- [5] F. Turco et al., *Phys. Plasmas*, 16(6):062301, 2009.
- [6] S. Coda et al., *Nucl. Fusion*, 47, 07, 2007.
- [7] P. A. Politzer et al., *Nucl. Fusion*, 45, 05, 2005.
- [8] F. Imbeaux et al., *Proc. of the 20th IAEA Fusion Energy Conference*, Vilamoura, Portugal, 2004.
- [9] A. Fukuyama, *Nucl. Fusion*, 35(12), 1995.
- [10] I. Voitsekhovitch and D. Moreau, *Nucl. Fusion*, 41(7):845864, 2001.
- [11] S. H. Strogatz, *Nonlinear Dynamics and Chaos*. Westview Press, 2000.
- [12] J. P. Freidberg, *Plasma physics and fusion energy*. Cambridge University Press, 2007.
- [13] J. Wesson, *Tokamaks*, *Oxford Science Publications*, 2001.
- [14] I. Voitsekhovitch et al., *Nucl. Fusion*, 37(12):17151733, 1997.
- [15] J. P. S. Bizarro et al., *Plasma Phys. Control. Fusion*, 58(10):105010, 2016.
- [16] J. P. S. Bizarro, L. Venâncio and R. V. Mendes, arXiv:1905.04520, 2019.